Supporting Information for "Crustal velocity variations and constraints on material properties in the Charlevoix Seismic Zone, eastern Canada"

J. Onwuemeka[1*], Y. Liu[1], and R. M. Harrington[2]

[1]Department of Earth and Planetary Sciences, McGill University, Montreal, Quebec, Canada

[2]Institute of Geology, Mineralogy and Geophysics, Ruhr University, Bochum, Germany

Contents of this file

1. Text S1 to S3
2. Figures S1 to S21

S1 Traveltime tomography and hypocenter relocation We jointly invert for hypocenter and velocity structure in the Charlevoix seismic zone using body wave phase traveltime information of 2405 earthquakes reported between January, 1988, and May, 2019. We perform robust synthetic (checkerboard) tests to quantify the capability of the inversion algorithm and ability of the data set to resolve velocity structure. Steps in the synthetic test include tests for influences of grid size parameterization, checkerboard size, source-station geometry, forward solver, and starting velocity models. The synthetic travel times were generated with the catalog source-station geometries and the forward solver implemented in *TomoDD*. The inversion was performed with *LOTOS* to eliminate potential biases and errors in the forward solver. The results show that the main features in the checkerboard were recovered irrespective of the grid size parameterization, source-station geometry, and starting velocity model. The checkerboard recovery inverted with velocity model shown in Figure S1b is the most impacted. The checkerboard recovery diminishes with decreasing checkerboard size due to decreasing ray density within the checkerboard cubes.

Following results of the synthetic test, we performed tomographic inversion with the real data with grid size parameterization of 1 km and the south shore velocity model of (Lamontagne, 1999), as they both yield the lowest RMS error for V_p and V_s. The relocated hypocenters are shown in Fig. S12. The map and cross-sectional views of the V_p/V_s models are

*Current address: Dept. of Earth and Planetary Sciences, McGill University, Montreal, Quebec, Canada

shown in Figs. S14 & S14. The cross-sectional profiles were chosen to highlight velocity variations with the highly damaged crust due to the meteorite impact and the surroundings. For example, profile EE' shows velocity variations outside the impact zone, whereas the NE-SW profiles are intended to show variations within and outside the impact structure on single profiles.

S2 Gravity predictions We calculate the synthetic residual Bouguer anomaly with the complete 3D density models determined from intense fracturing and compositional variation scenarios. The 3D density models are divided into 3D voxels of the same grid spacing as the tomographic model. Each voxel in the 3D models is approximated by a sphere and the gravitational anomaly of each spherical mass point is calculated with in the wavenumber domain using the following expression, respectively (Li, 2010; Schmidt et al., 2010, 2011):

$$\mathcal{F}[g(\mathbf{K})] = 2\pi G\mathcal{F}[\Delta\rho(\mathbf{K})] \tag{1}$$

where G, $\Delta\rho$, R, and x, y, z, F, and $\mathbf{K}$ are the gravitational constant, density contrast, radius of sphere, and components of distance between mass point location and observation point (i.e. gravity station), Fourier transform, and wavenumber vector, respectively. In the wavenumber domain, each voxel is divided into a number of horizontal laminas that represent density sheets. The gravitational attraction of each laminae is calculated with a Fast Fourier Transform (FFT), filtered, and transferred to spatial domain with the inverse FFT. The vertical gravitational component of all the laminas in a voxel is summed to derived the vertical gravity component of the voxel.

The observed gravity anomalies were rediscretized to match the grid size and spacing of the model (Fig. S15). The best 5 predicted gravity anomalies that more closely match observed residual Bourguer anomaly for both scenarios is shown in Figures S18 - S21.

S3 Data and model limitations The traveltime data set contains a mix of manual and automatic arrival time picks. The traveltime data are retrieved from the Geological survey of Canada (GSC) and (Yu et al., 2016), whereas the rest of the arrival time data were manually picked by the authors. Due to data sparsity within the upper 2 km, tomography result for depths less than 2 km are less well-constrained. The neural network does not return a 100% cross-validation score for any of the model, hence some of

the predicted densities may be slightly different from the input (Fig. S17). The cross-validation scores were not less than 80% and the neural network predicted most of the major gravity anomalies in the observation (Figs. S18 & S20), hence, density prediction error are within tolerable limits.

References

Lamontagne, M. (1999). Rheological and geological constraints on the earthquake distribution in the charlevoix seismic zone, quebec, canada. *Ph.D. thesis, Carleton University, (Geological Survey of Canada Open File Report D-3778)*.

Li, X. (2010). Efficient 3d gravity and magnetic modeling. In *Proceedings of egm 2010 international workshop.*

Schmidt, S., Götze, H.-J., Fichler, C., & Alvers, M. (2010). Igmas+–a new 3d gravity, ftg and magnetic modeling software. *GEO-INFORMATIK Die Welt im Netz, edited by: Zipf, A., Behncke, K., Hillen, F., and Scheffermeyer, J., Akademische Verlagsgesellschaft AKA GmbH, Heidelberg, Germany*, 57–63.

Schmidt, S., Plonka, C., Götze, H.-J., & Lahmeyer, B. (2011). Hybrid modelling of gravity, gravity gradients and magnetic fields. *Geophysical Prospecting*, *59*(Advances in Electromagnetic, Gravity and Magnetic Methods for Exploration), 1046–1051.

Yu, H., Liu, Y., Harrington, R. M., & Lamontagne, M. (2016). Seismicity along st. lawrence paleorift faults overprinted by a meteorite impact structure in charlevoix, québec, eastern canada. *Bulletin of the Seismological Society of America*, *106*(6), 2663–2673.

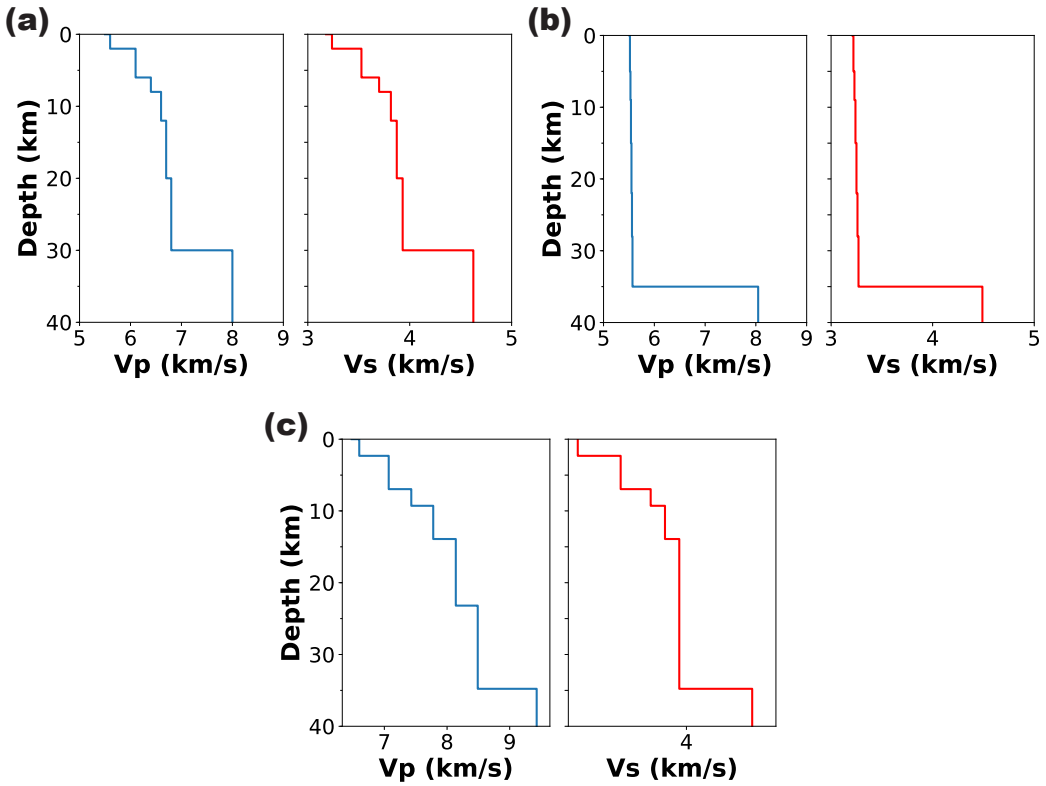

Figure S1. (a) The south shore velocity model of Lamontagne (1999). (b) a quasi layer-over-halfspace velocity model. (c) A perturbed velocity model determined by randomised perturbation of (a).

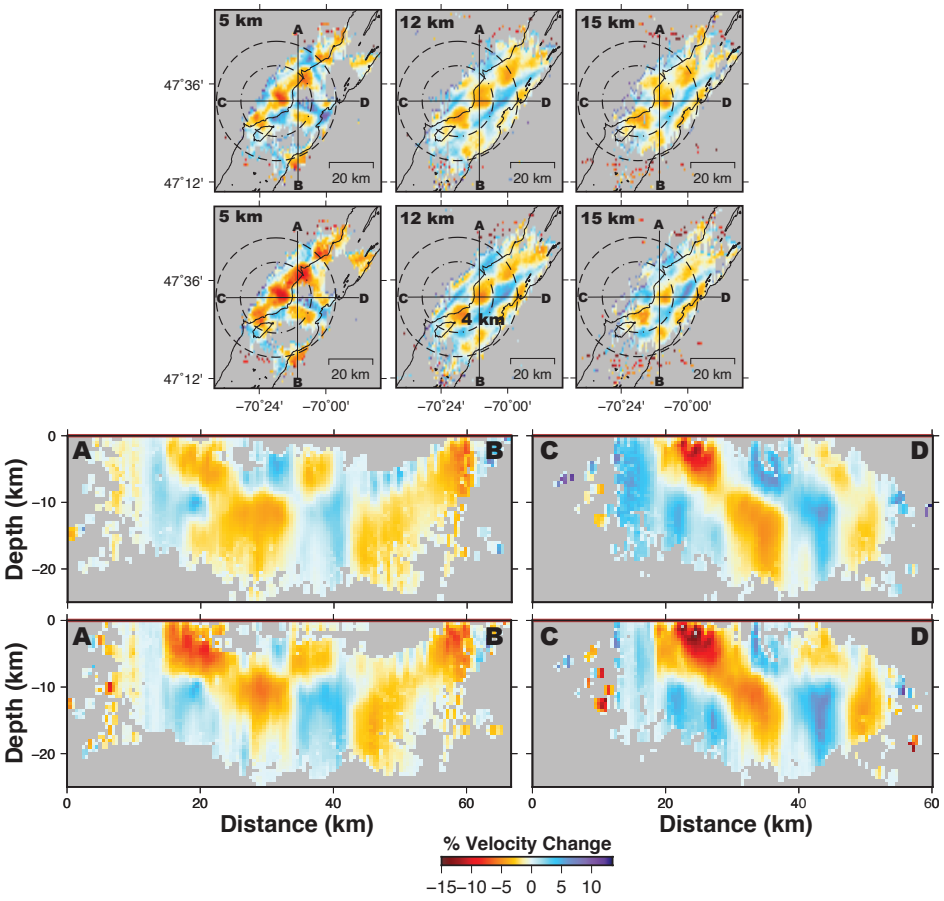

Figure S2. Checkerboard recovery with grid size parameterization of 0.5 km.

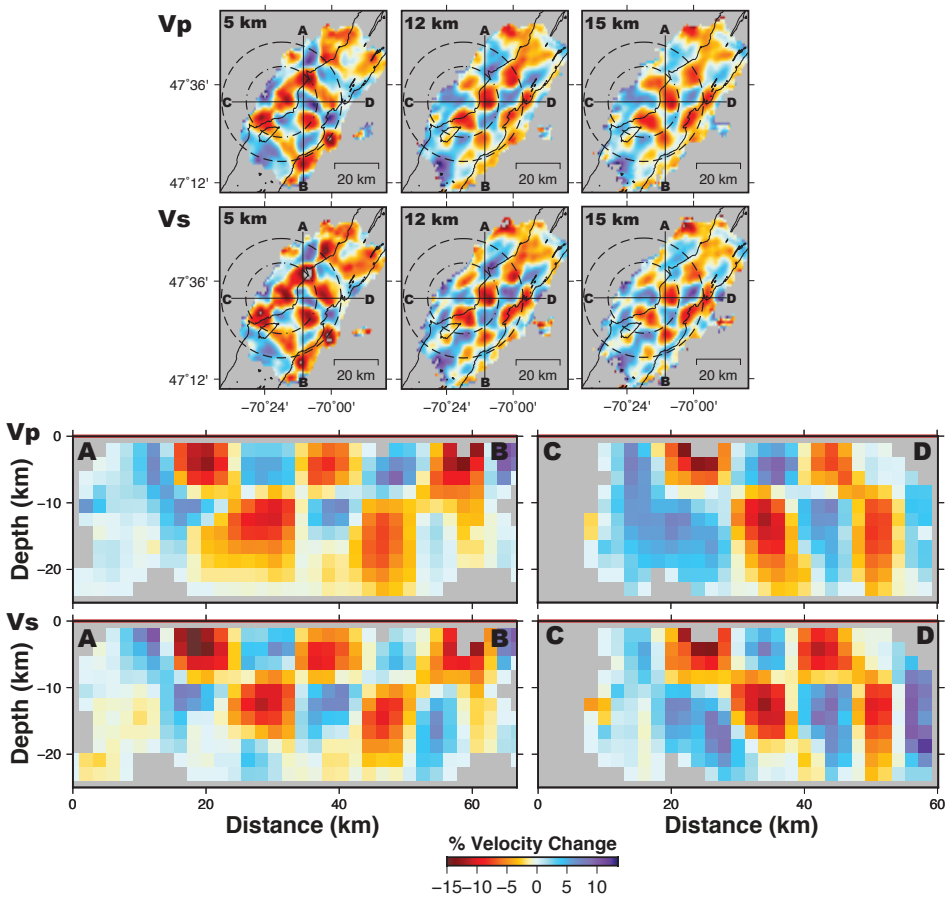

Figure S3. Checkerboard recovery with grid size parameterization of 2 km.

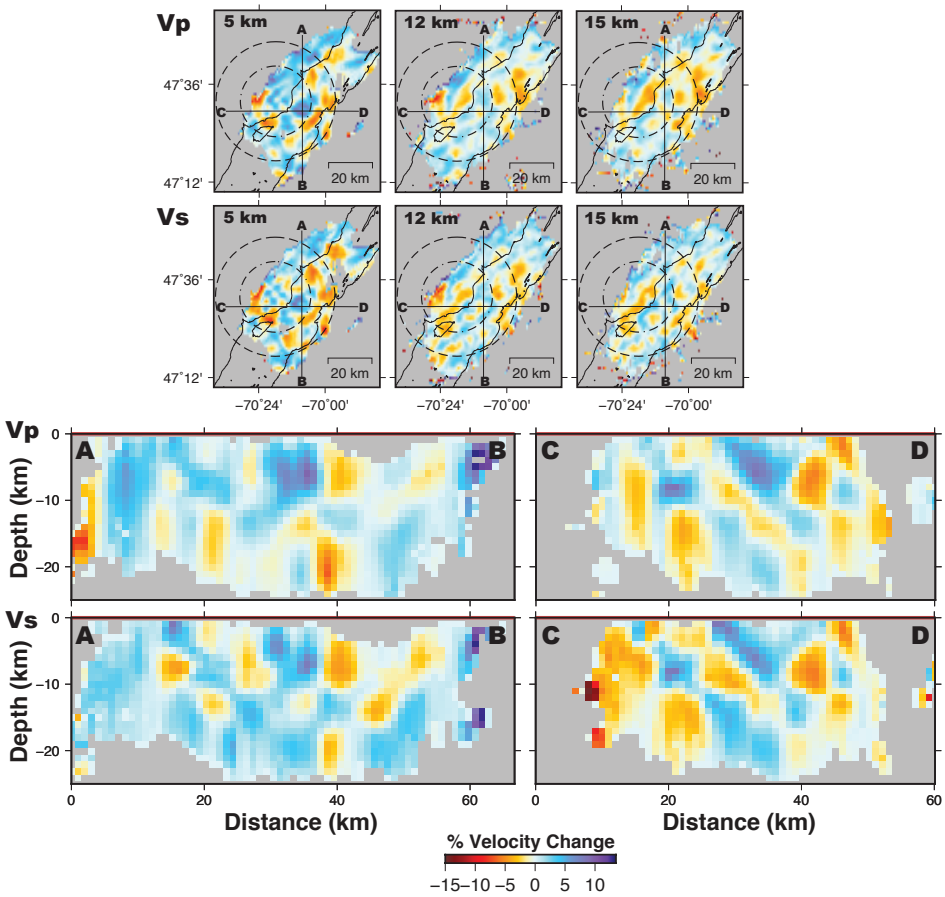

Figure S4. Checkerboard recovery for 6 km checkerboard size and grid size parameterization of 1 km.

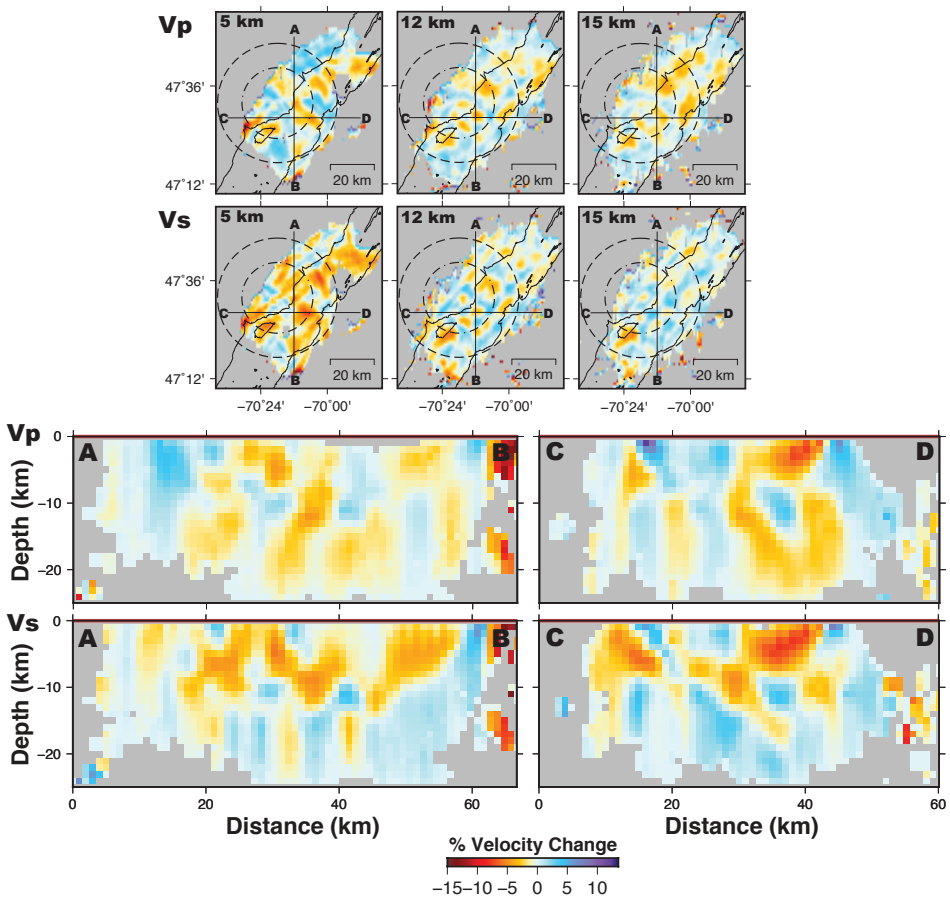

Figure S5. Checkerboard recovery for 5 km checkerboard size and grid size parameterization of 1 km.

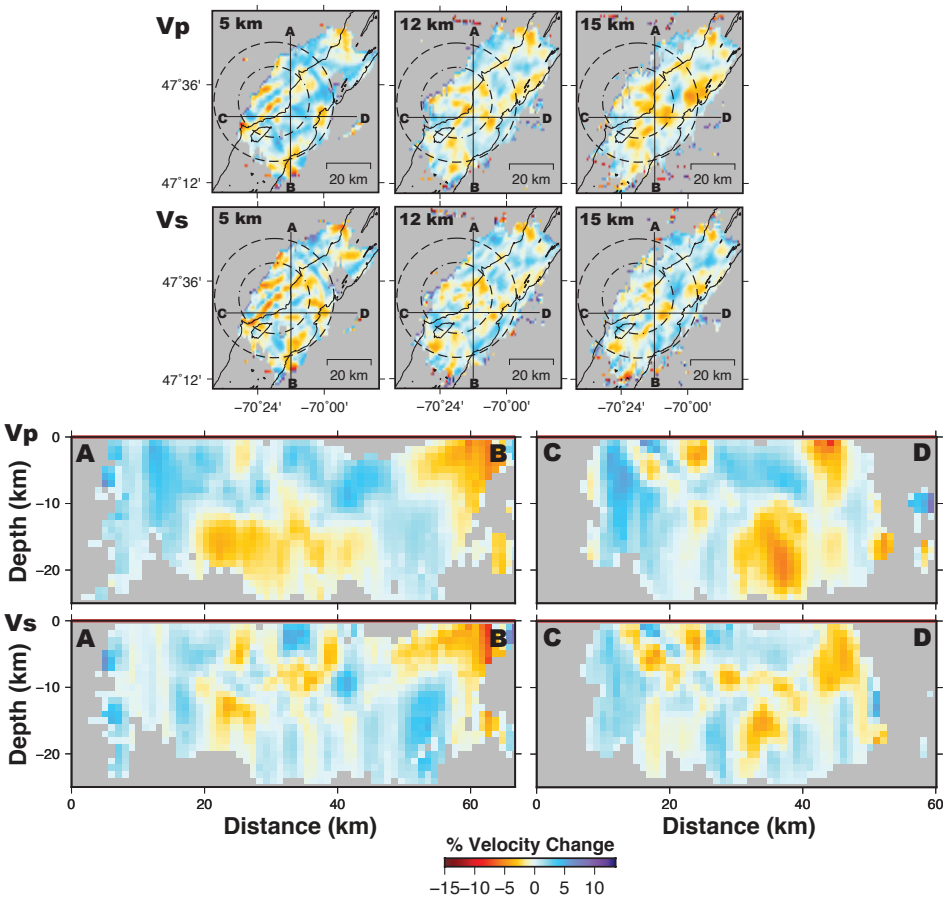

Figure S6. Checkerboard recovery for 4 km checkerboard size and grid size parameterization of 1 km.

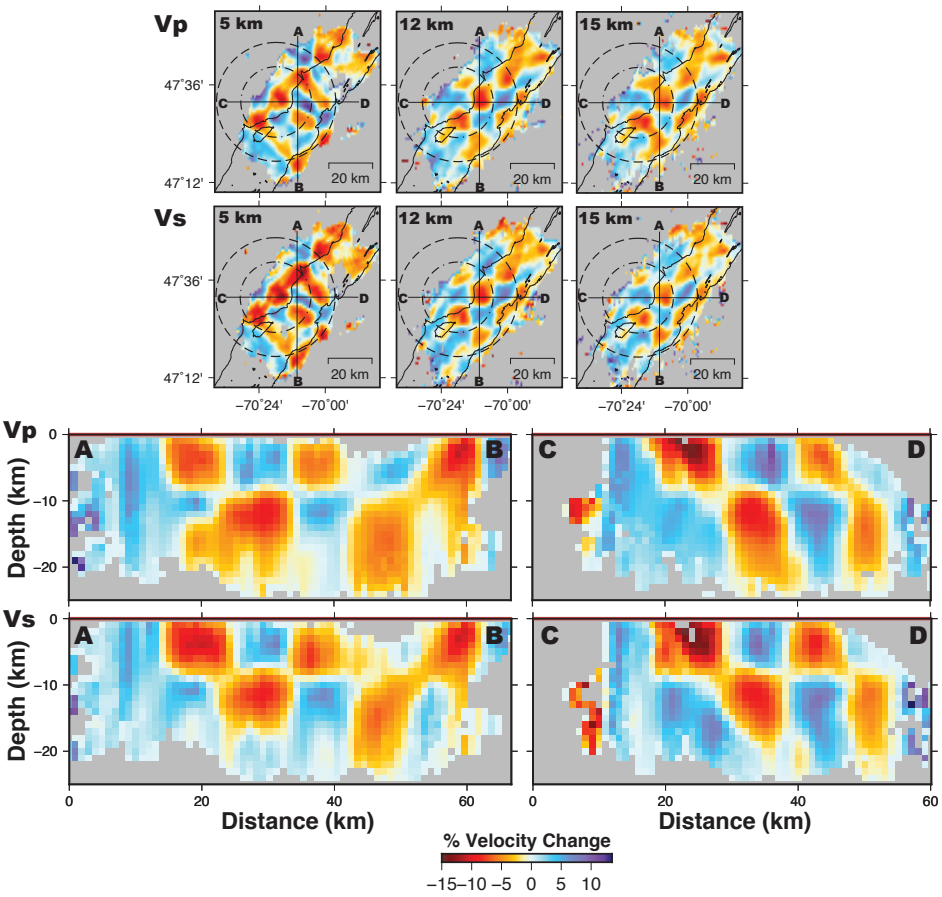

Figure S7. Checkerboard recovery for 10 km checkerboard size and grid size parameterization of 1 km. All the events are placed at 1 km depth in the middle of the study area.

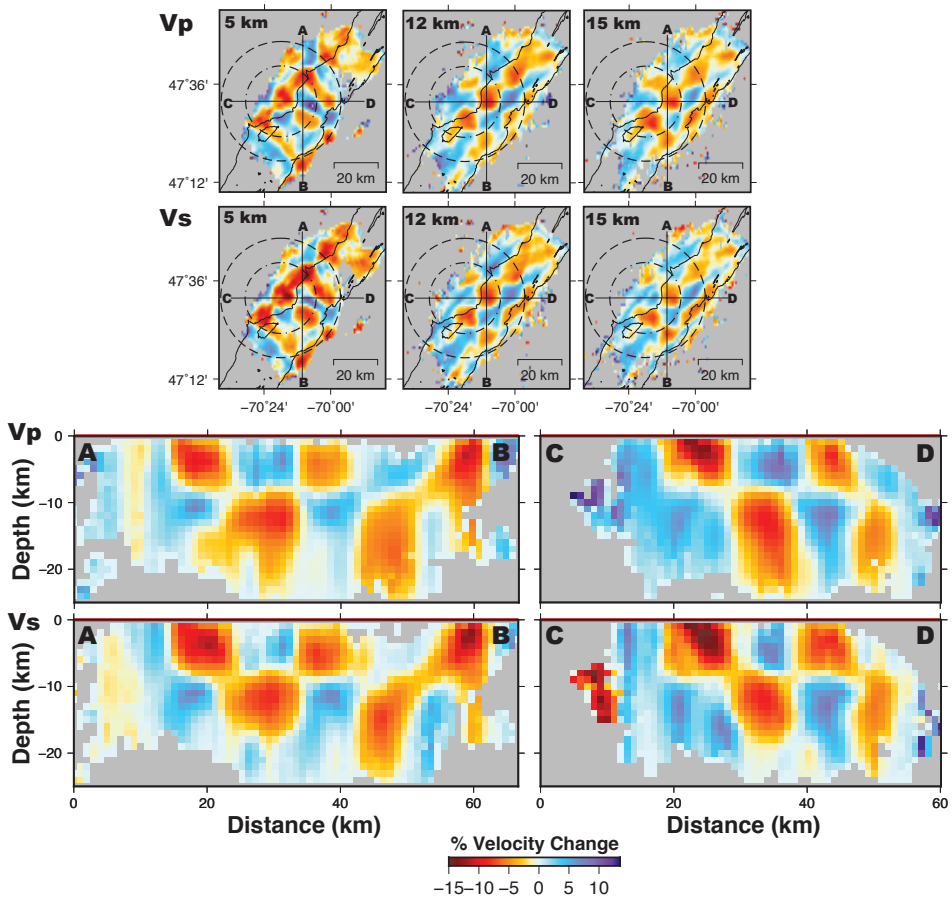

Figure S8. Checkerboard recovery for 10 km checkerboard size and grid size parameterization of 1 km. All events are initially placed at 5 km depth in the middle of the study area.

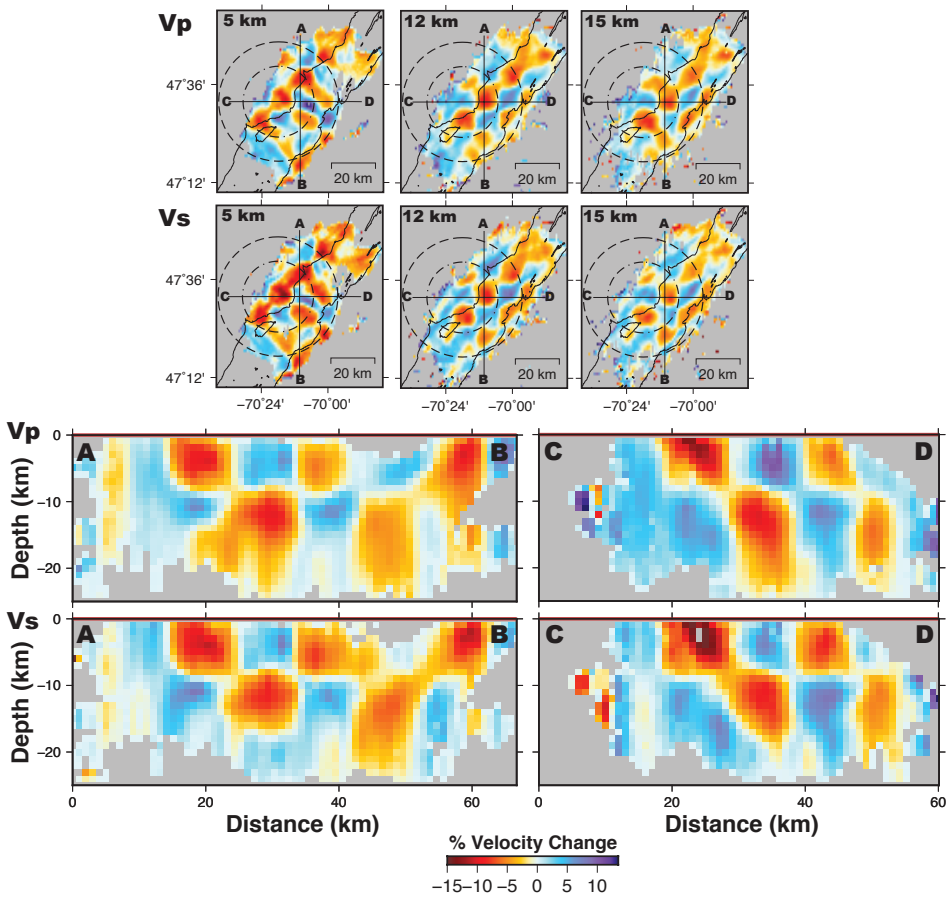

Figure S9. Checkerboard recovery for 10 km checkerboard size and grid size parameterization of 1 km. All events are initially placed at 10 km depth in the middle of the study area.

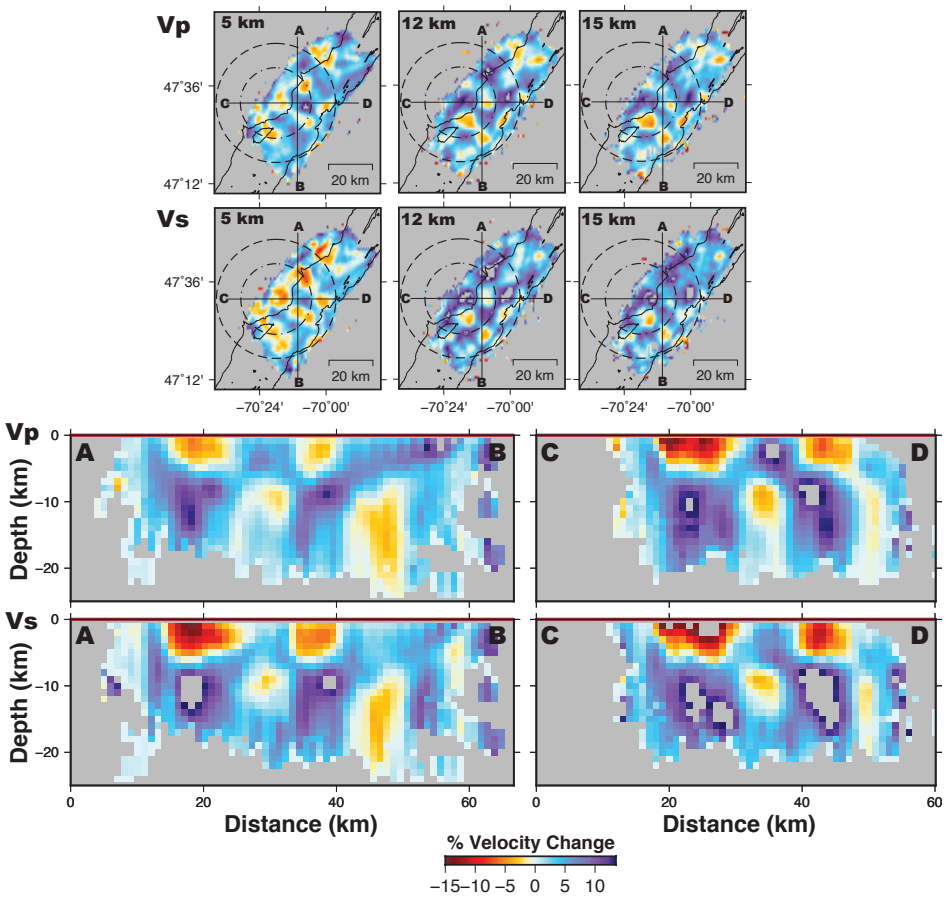

Figure S10. Checkerboard recovery for 10 km checkerboard size, grid size parameterization of 1 km, and starting velocity model Fig. S1b.

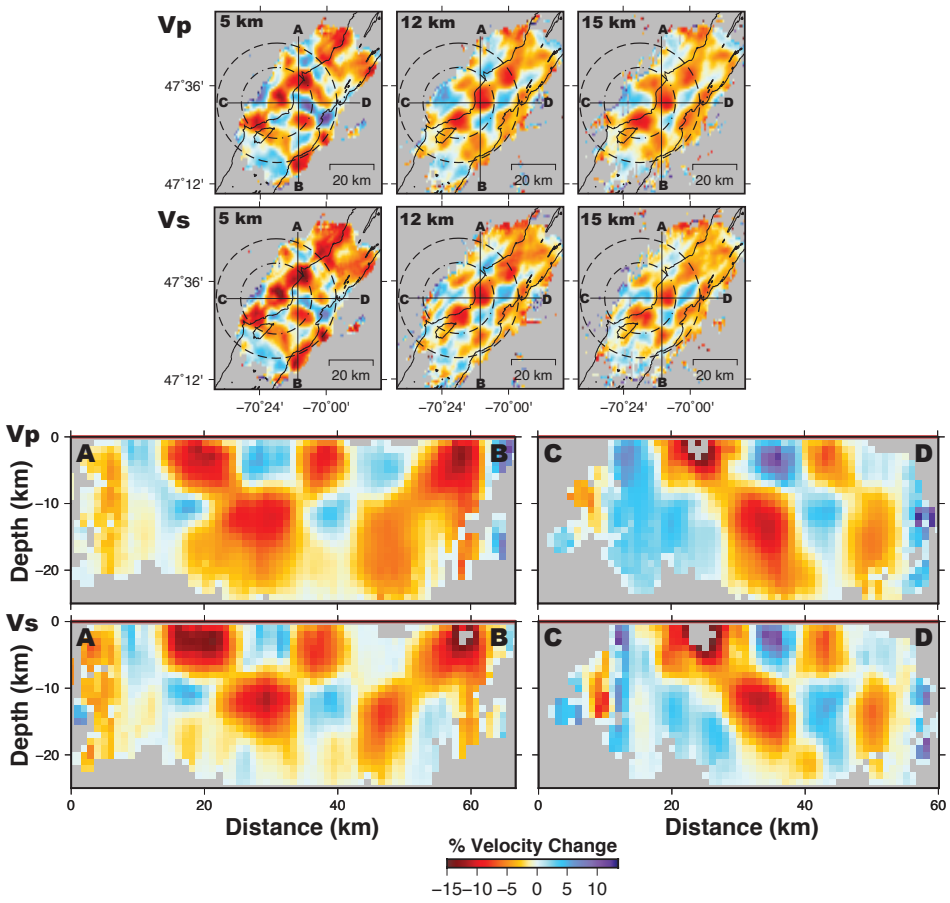

Figure S11. Checkerboard recovery for 10 km checkerboard size, grid size parameterization of 1 km, and starting velocity model Fig. S1c.

Figure S12. Relocated hypocenters of 1557 earthquakes in the study area.

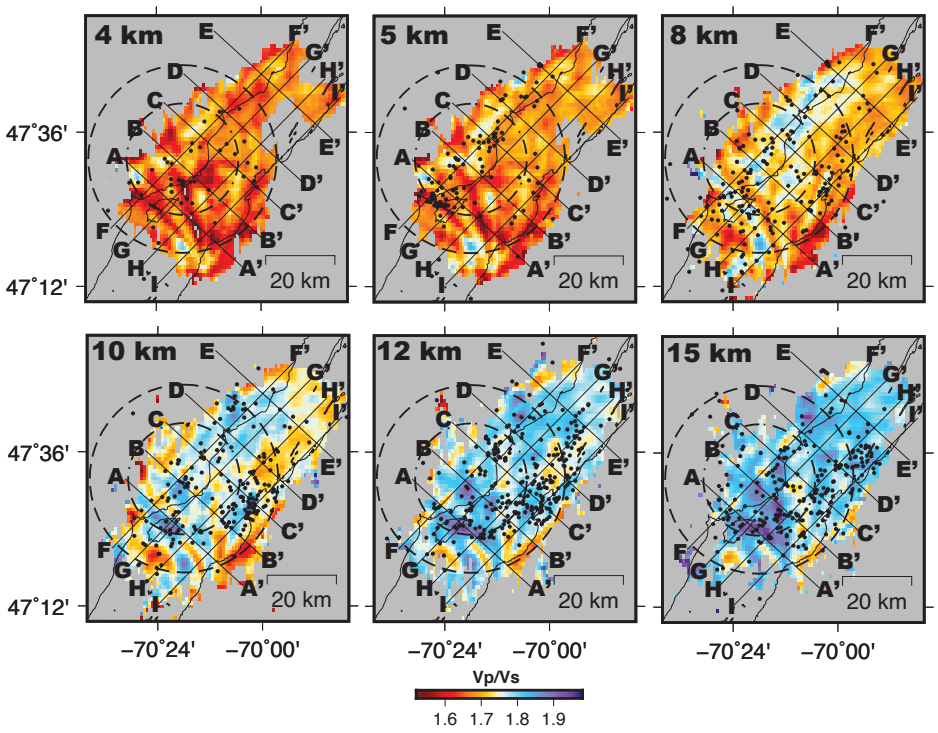

Figure S13. Map view of V_p/V_s variation.

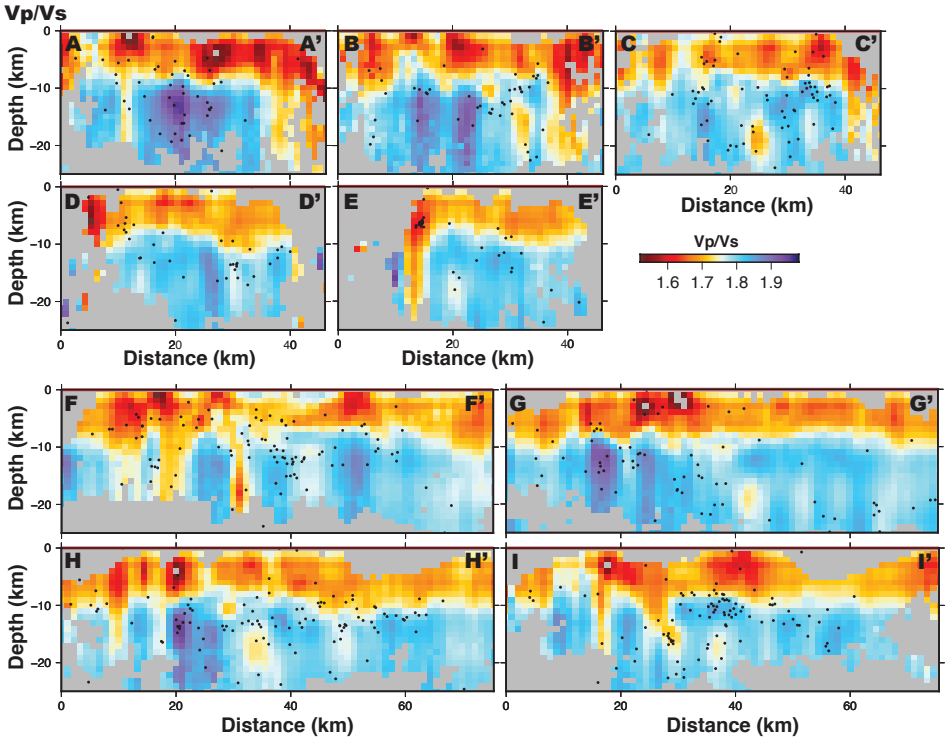

Figure S14. Cross-sectional view of V_p/V_s variation.

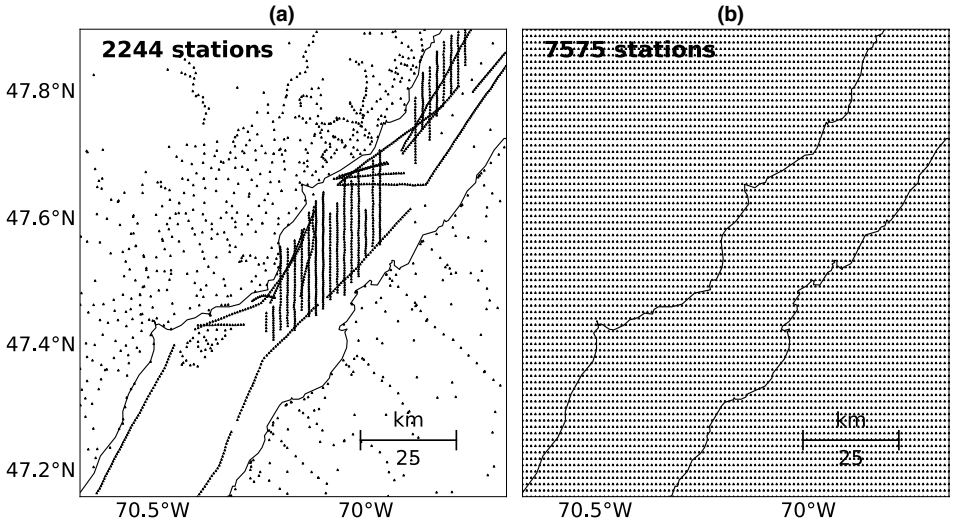

Figure S15. (a) Original Bouguer anomaly data points. (b) Interpolated Bouguer anomaly data points.

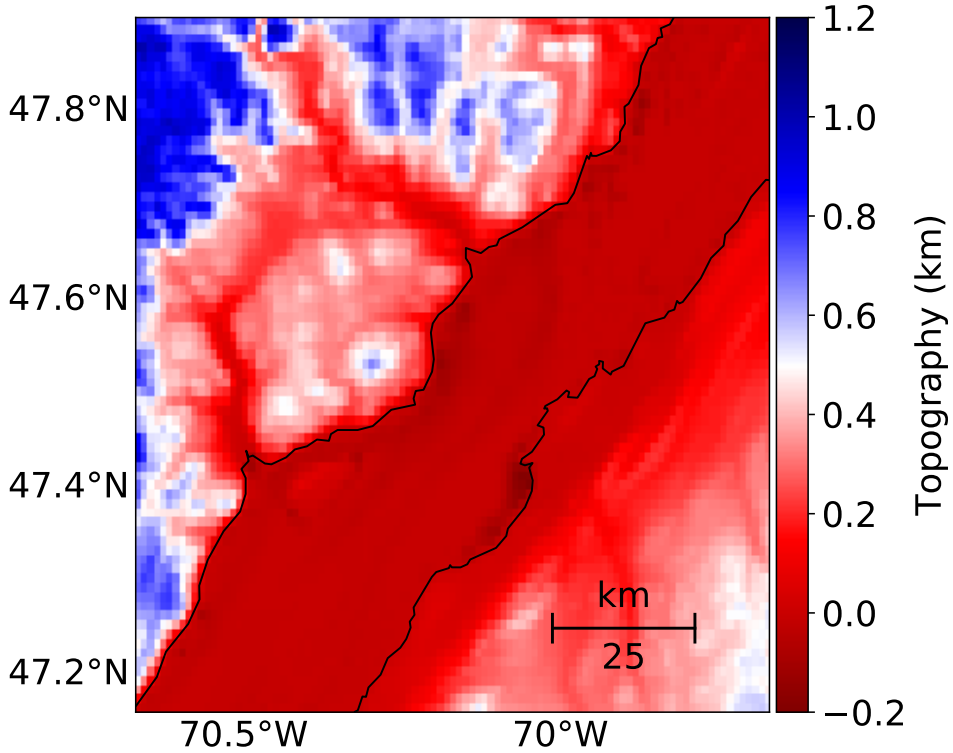

Figure S16. Topography map of the study area.

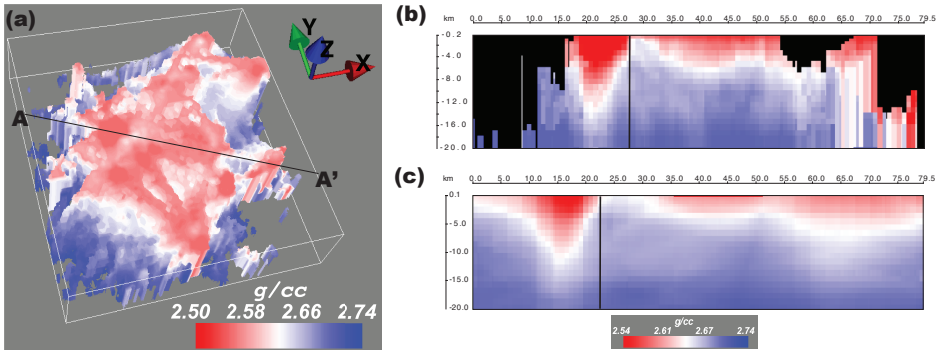

Figure S17. (a) Same as in Fig. 9a. (b) Cross-sectional view of densities along profile AA' before MPL regression. (c) Cross-sectional view of densities along profile AA' after MPL regression. The vertical black lines in (b) & (c) highlight a $\sim$ 5 km shift of the low-density body to the left of the lines.

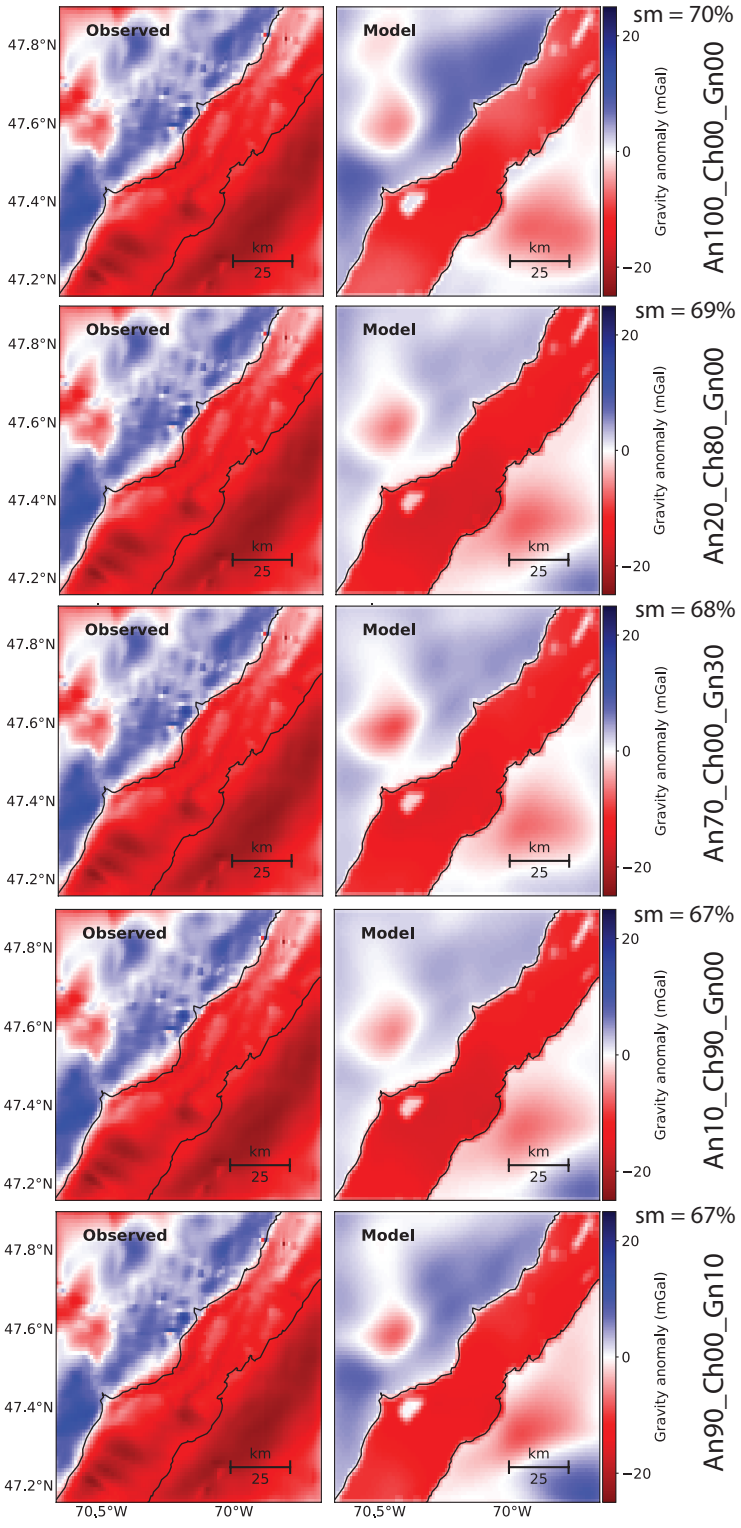

Figure S18. The five best predicted gravity anomalies of the entire study area for the intense fracturing scenario. The percent composition of the 3 rock types and similarity measure (sm) of the fits are indicated.

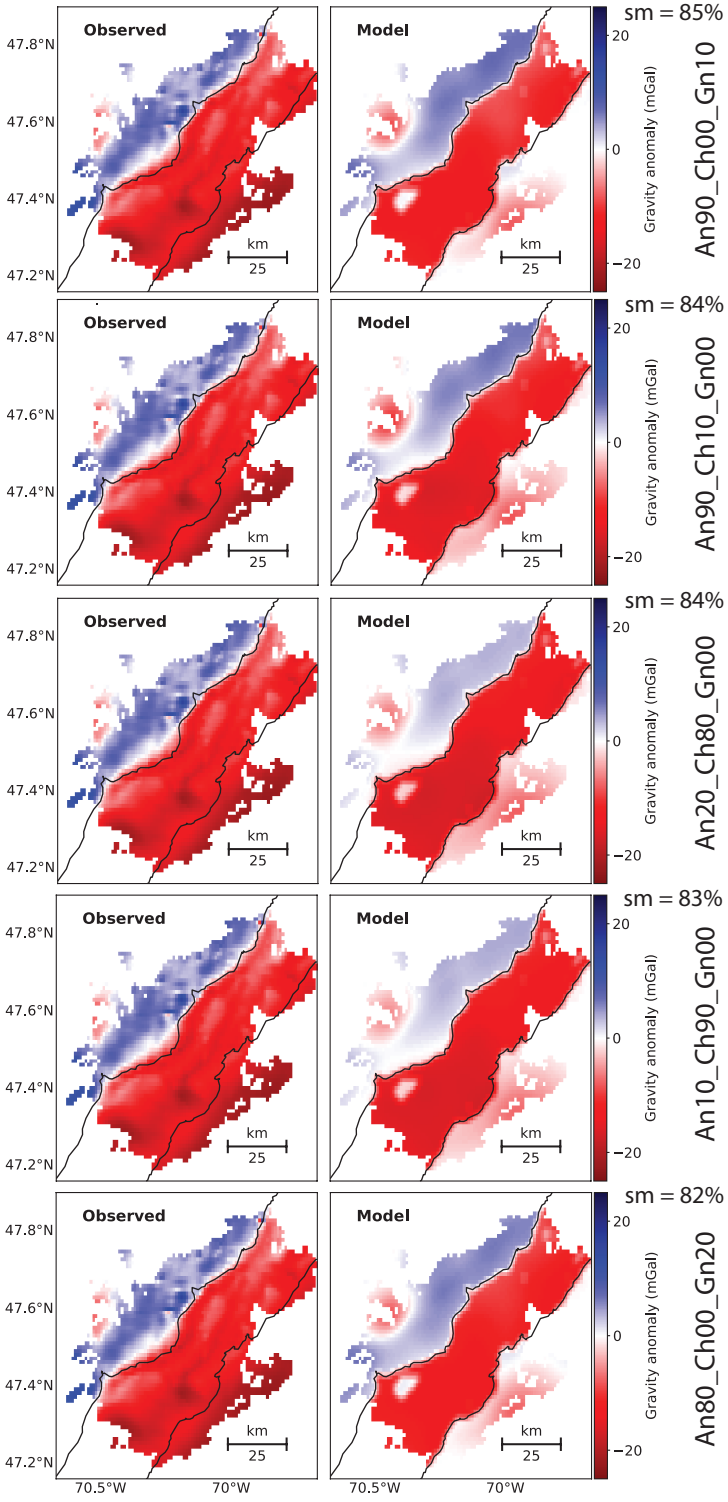

Figure S19. The five best predicted gravity anomalies of the section of the study area with dense ray coverage for the intense fracturing scenario. The percent composition of the 3 rock types and similarity measure (sm) of the fits are indicated.

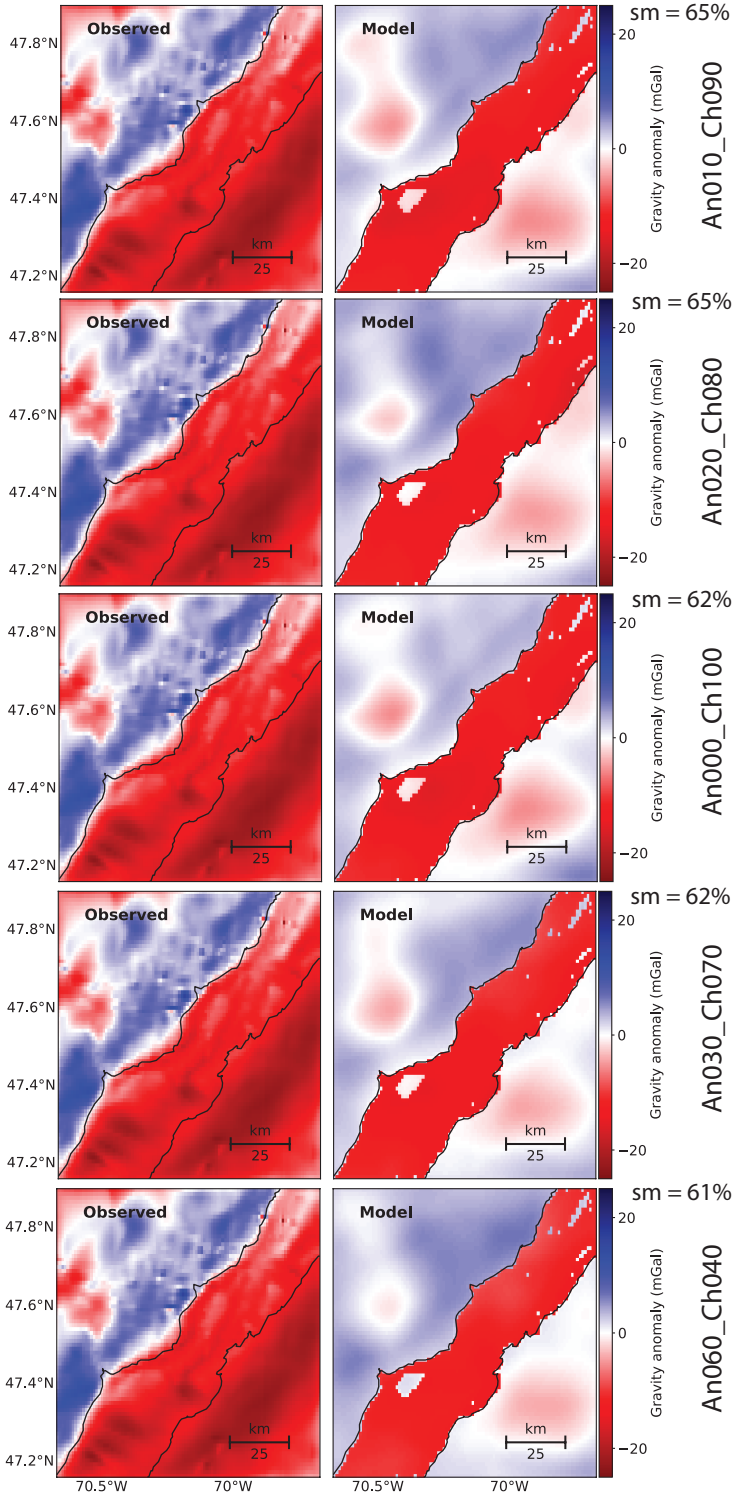

Figure S20. The five best predicted gravity anomalies of the entire study area for the compositional variation scenario. The percent composition of anorthosite and charnockite in the composite rock (i.e. phase 1) and similarity measure (sm) of the fits are indicated.

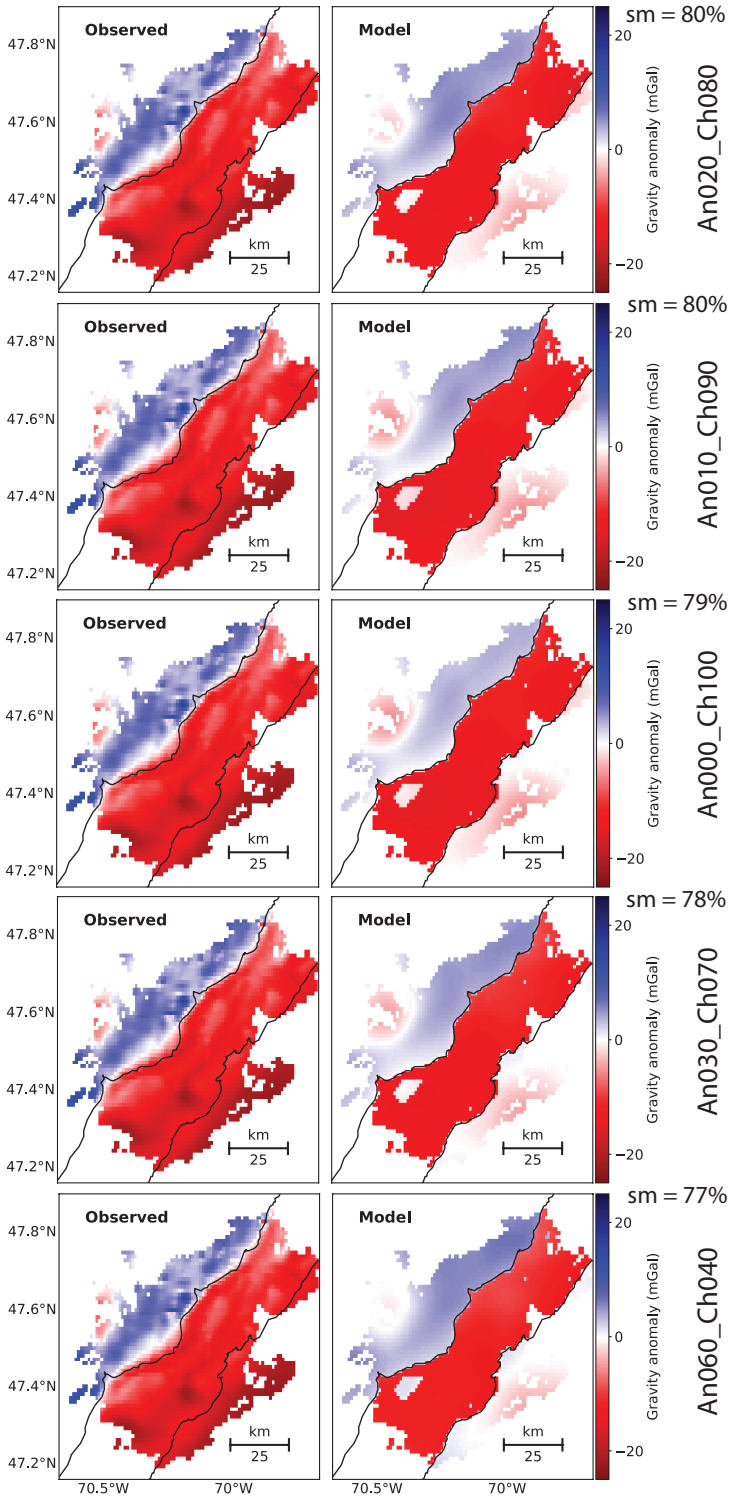

Figure S21. The five best predicted gravity anomalies of the section of the study area with dense ray coverage for the compostional variation scenario. The percent composition of anorthosite and charnockite in the composite rock (i.e. phase 1) and similarity measure (sm) of the fits are indicated.